Interfacial control of domain structure and magnetic anisotropy in La$_{0.67}$Sr$_{0.33}$MnO$_3$ manganite heterostructures

Da Lan [1], Pingfan Chen,[1] Chao Liu,[1] Xiaohan Wu,[1] Ping Yang,[2] Xiaojiang Yu [2], Jun Ding,[1]
Jingsheng Chen,[1] and Gan Moog Chow [1,*]

[1]*Department of Materials Science and Engineering, National University of Singapore, 117575 Singapore*
[2]*Singapore Synchrotron Light Source (SSLS), National University of Singapore, 5 Research Link, 117603 Singapore*

Structural domains in ferroic materials can be manipulated to achieve novel properties and functionalities of devices with multiple tunabilities. Herein, we report a study of tunable domain structures in ferroelastic La$_{0.67}$Sr$_{0.33}$MnO$_3$ (LSMO) films via interfacial engineering. Distinct domain structures are formed in rhombohedral LSMO films depending on the crystallographic orientations of the orthorhombic NdGaO$_3$ (NGO) substrates. A unidirectional lattice modulation is observed in LSMO films grown on NGO(110)$_{Or}$ substrates, whereas a unidirectional twinned-domain structure is generated by NGO(001)$_{Or}$ substrates (where Or in the subscript denotes orthorhombic notation). The orientation-dependent domain structures in LSMO films are controlled by anisotropic strain as well as interfacial oxygen octahedral coupling at the heterointerface between LSMO and NGO. The orbital occupancy and in-plane magnetic anisotropy are markedly affected by strain relief induced by the unidirectional structural domains in LSMO films. In addition, the structural results observed in LSMO/NGO(001)$_{Or}$ films further demonstrate that anisotropic strain is capable to disturb octahedral connectivity in epitaxial films. Our findings provide future directions to understand and control the domain structures in ferroelastic heterostructures of perovskite materials and open a pathway towards tailoring the desirable physical properties.

I. INTRODUCTION

As the largest class of ferroic materials, ferroelastics, which possess a non-Hookean strain-stress response, have attracted tremendous interests in both fundamental research as well as technological applications [1–3]. Complex perovskite oxides with a rhombohedral lattice structure are prototypical ferroelastic materials, which are of particular interest due to a diverse range of physical phenomena spanning from colossal magnetoresistance to metal-to-insulator transition and multiferroicity [4–6]. The rhombohedral perovskite structure is derived from the undistorted cubic structure by compression of the [111] direction, leading to the ferroelastic response. To reduce the total elastic energy, ferroelastic oxide films generally form twinned domains [7–9]. The interplay between the spin, orbital, charge orders, and lattice structure in strongly correlated oxide films makes the structural domain a pivotal factor in tailoring the physical properties [8,10–15]. For example, altering the miscut angle of SrTiO$_3$ (STO) substrates can tune the domain structure in ferroelectric films and subsequently modify the ferroelectric properties, such as ferroelectric switching behavior, leakage current, and coercive field [12,13]. Likewise, by controlling the domain structure, unexpected in-plane anisotropy of orbital configuration and magnetization are achieved in ferromagnetic films [1]. Understanding of the manipulation of the domain structure will

provide an effective approach to modify the physical properties of strongly correlated oxides.

Recent advances in oxide epitaxy have enabled the synthesis of high-quality heterostructures with atomic-scale control. Various novel phenomena and functionalities that are unattainable in the bulk materials emerge at the complex oxide heterointerfaces due to cooperation/competition of different interfacial phenomena, such as charge transfer, polar discontinuity, orbital polarization, spatial confinement, etc. [16–18]. Two-dimensional electron gas between two band insulators [18,19], exchange bias in an antiferromagnet/paramagnet system [20,21], magnetoelectric coupling at the interface between a ferroelectric and a ferromagnet [22,23], and antiferromagnetic coupling between two ferromagnets [24,25] are only a few examples of the active fields of research on dominant interfacial effects of perovskite heterostructures. Specifically, the epitaxial growth of the ABO$_3$ perovskite films makes it possible to trigger a lattice distortion of the films via structural proximity effect between the film and substrate, while in bulk materials the lattice distortions can be only varied by applying hydrostatic or chemical pressure. Epitaxial strain and interfacial oxygen octahedral coupling have been considered as two of the most important means to control structural behavior in the epitaxial films allowing for the stabilization of local atomic structures distinct from the equilibrium bulk counterparts [26–29]. On one hand, epitaxial strain can have a notable effect on the BO$_6$ bonding environment, as the substrate in-plane lattice parameters are imposed on the film, yielding BO$_6$ distortion and/or rotations that are inaccessible in compositionally equivalent bulk

compounds [28]. On the other hand, a symmetry mismatch or a difference in the magnitude of octahedral rotations at a coherent heterointerface provides an alternative means to modify local atomic structure. To maintain the corner connectivity of the BO_6 octahedra across an interface, the octahedral rotations near a perovskite heterointerface are tailored. For instance, rotations are suppressed in the near-interfacial region of orthorhombic or rhombohedral perovskites epitaxially constrained to cubic perovskites [30,31]. Therefore, fabricating artificial heterostructures comprising ferroelastic complex oxides provides opportunities for designing and tuning the domain structures in the ferroelastic film, benefiting from the structural proximity effect between the film and the underlying substrate or buffer layer.

As a prototypical oxide ferroelastic, $La_{0.67}Sr_{0.33}MnO_3$ (LSMO) has attracted immense attention over the past decades due to its intriguing properties, for example, colossal magnetoresistance, half metallicity with 100% spin polarization, and room-temperature ferromagnetism [32,33]. Bulk LSMO possesses a rhombohedral structure with the pseudocubic unit length $a_{PC} = 3.878$ Å and rhombohedral angle 90.39 °, where the subscript PC in the indices stands for the pseudocubic notation [34]. Accordingly, when LSMO is heterostructured with the cubic substrate, the lattice misfit of the rhombohedral structure relative to the cubic substrate can be divided into two contributions: (i) biaxial strain induced by the lattice mismatch, and (ii) shear strain induced by the angle mismatch (see Fig. S1 of the Supplemental Material [35]). Under the shear strain, LSMO films form structural domains, that can in turn relax the shear strain [36]. Such domains have been observed by transmission electron microscopy and high-resolution x-ray-diffraction (HR-XRD) measurements [7,8,37–39]. For instance, checkerboardlike domain structures are formed in $LSMO/(LaAlO_3)_{0.3}(Sr_2AlTaO_6)_{0.7}$ (LSAT) and LSMO/STO films [8,40]. When STO substrates were modified with miscut angles, anisotropic domain stripes along the surface step terraces were formed in LSMO films.

Similarly, an anisotropic domain structure was generated in LSMO epitaxial films by orthorhombic $NdGaO_3$ substrates with $(110)_{Or}$ orientation (the subscript Or in the index denotes the orthorhombic notation), where oxygen octahedral distortions and anisotropic strain exist [41]. Though the oxygen octahedral distortions and anisotropic strain play crucial roles in determining the domain structure in LSMO films, the details of cooperation and competition of these effects are not fully understood for the modulation of domain structure [41]. Therefore, further understanding of the effects of octahedral distortion and anisotropic strain on the domain structure in LSMO films grown on an orthorhombic substrate is warranted.

In this work, NGO single crystal is selected as the orthorhombic substrate. By varying the crystallographic orientation of the NGO substrates from $(110)_{Or}$ to $(001)_{Or}$, the domain structures in LSMO layers are investigated. The observed unidirectional lattice modulation and unidirectional twinned domain in $(110)_{Or}$- and $(001)_{Or}$-oriented LSMO films demonstrate that not only the shear strain but also the anisotropic strain and octahedral proximity effect play central parts in the formation of ferroelastic structural domains. By analyzing the origin of the distinct domain structures,

a deeper understanding on how the anisotropic strain and octahedral proximity effect affect the domain structures in LSMO films is obtained. More strikingly, the orbital occupancy of Mn e_g electrons as well as the in-plane magnetic anisotropy of LSMO films are pronouncedly influenced by the unidirectional structural domains. This modulation of orbital occupancy and in-plane magnetic anisotropy is ascribed to the partially relieved anisotropic strain in LSMO films induced by the unidirectional structural domains. Our work demonstrates the strong correlation between domain structures and interfacial oxygen octahedral coupling as well as anisotropic strain in ferroelastic films, and their effects on magnetic properties.

II. EXPERIMENT

LSMO single films and LSMO/STO bilayers were deposited onto $NGO(110)_{Or}$ and $NGO(001)_{Or}$ substrates using pulsed laser deposition (PLD) with *in situ* reflection high-energy electron diffraction. The LSMO layers and STO layers were grown under an oxygen partial pressure of 200 and 100 mTorr, respectively. The substrate temperature was maintained at 750 °C during the deposition. LSMO and STO polycrystalline targets were ablated by a KrF excimer laser ($\lambda = 48$ nm; Coherent) with a laser fluence of ~ 2 J/cm^2. The laser repetition rate was set at 3 Hz. After film growth, pure oxygen (typically 100 Torr annealing for 0.5 h) was introduced to the PLD chamber, and the samples were cooled down to room temperature at a cooling rate of 10 °C min^{-1} to reduce oxygen vacancy. The crystal structures were characterized by HR-XRD using the Huber four-circle diffractometer system 90000–0216/0 at the Singapore Synchrotron Light Source (SSLS), with x-ray wavelength $\lambda = 1.5406$ Å.

All the magnetic measurements were conducted on a superconducting quantum interference device vibrating sample magnetometer (Quantum Design). The samples were first zero-field cooled to 100 K before conducting the measurements. During the measurements, the magnetic field (H) was applied along the in-plane $[100]_{PC}$ and $[001]_{PC}$ axes for the films grown on $NGO(110)_{Or}$ substrates, whereas H was applied along the in-plane $[110]_{PC}$ and $[1\bar{1}0]_{PC}$ axes for the films grown on $NGO(001)_{Or}$ substrates. For each magnetic hysteresis loop, the paramagnetic background from the NGO substrate is subtracted.

X-ray absorption spectroscopy (XAS) measurements were performed at the Surface, Interface, and Nanostructure Science beamline of the SSLS. The energy resolution was set ≈ 0.25 eV. XAS signals were recorded at room temperature from the total electron yield (TEY) current, which takes into account the surface sensitivity and element selectivity of the TEY mode. The x-ray linear dichroism (XLD) signal is obtained by subtracting the intensities of the linear-polarized x rays with out-of-plane (I_{out}) polarization from in-plane (I_{in}) polarization without magnetic field, that is, XLD = I_{in}-I_{out}.

III. RESULTS AND DISCUSSION

A. Contrasting domain structures in LSMO films grown on NGO substrates with various orientations

For convenience, pseudocubic indices are exploited for the orthorhombic NGO, with $[100]_{PC}$, $[010]_{PC}$, and $[001]_{PC}$
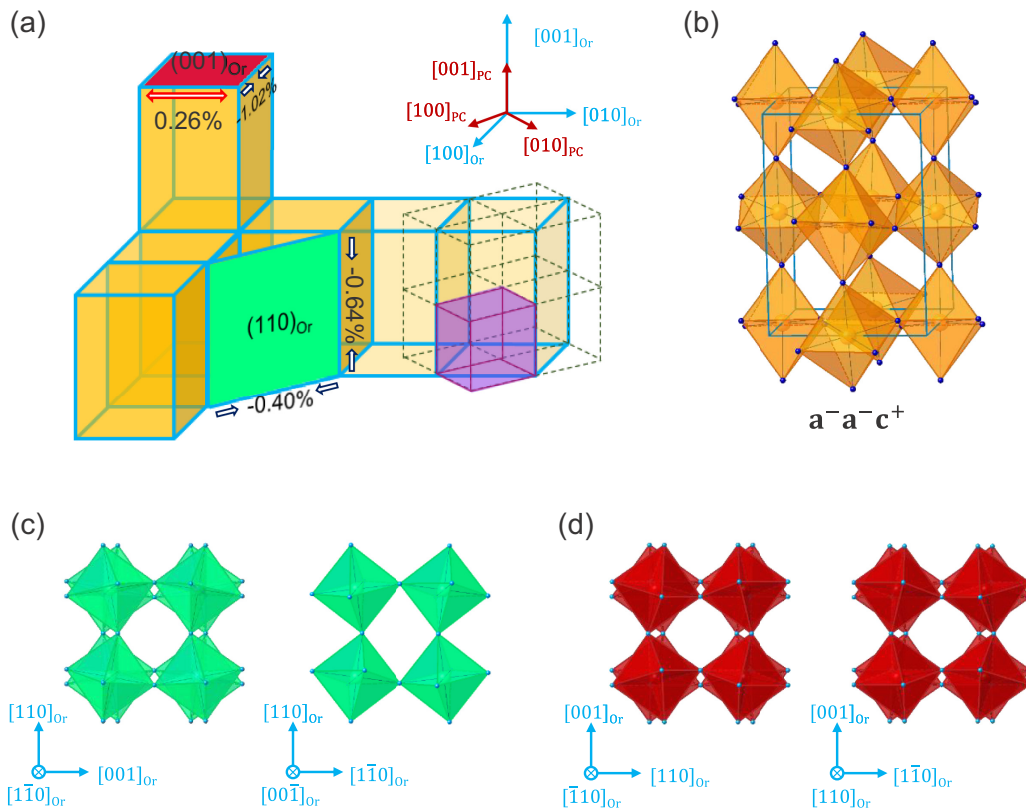
FIG. 1. Schematic diagram of orthorhombic NGO single crystal. (a) Strain states of the $La_{0.67}Sr_{0.33}MnO_3$ film received from the NdGaO$_3$ substrate at various orientations, and the relationship between the orthorhombic coordinate system and pseudocubic coordinate system. (b) Schematic of the orthorhombic *Pbnm* structure of NGO with $a^-a^-c^+$ rotation pattern. Schematics of the oxygen octahedral rotation of the (c) $(110)_{Or}$- and (d) $(001)_{Or}$-oriented NGO substrates viewed along different in-plane axes (as denoted).

pseudocubic axes corresponding to $[1\bar{1}0]_{Or}$, $[110]_{Or}$, and $[001]_{Or}$ orthorhombic axes, respectively [Fig. 1(a)]. The NGO substrates possess an $a^-a^-c^+$ rotation with the in-phase rotation along the $[001]_{PC}$ axis and out-of-phase rotations along the $[100]_{PC}$ and $[010]_{PC}$ axes, leading to the orthorhombic structure with the lattice parameters of $a_{Or} = 5.431$ Å, $b_{Or} = 5.499$ Å, and $c_{Or} = 7.710$ Å, as shown in Fig. 1(b) [42]. For the $(110)_{Or}$-oriented NGO substrate the oxygen octahedral rotation (OOR) pattern can be decomposed into in-plane $a^-a^0c^+$ rotation and out-of-plane $a^0a^-c^0$ rotation [Fig. 1(c)], whereas the OOR pattern of NGO$(001)_{Or}$ comprises in-plane $a^-a^-c^0$ rotation and out-of-plane $a^0a^0c^+$ rotation [Fig. 1(d)]. In contrast, the rhombohedral LSMO possesses an $a^-a^-a^-$ rotation with out-of-phase rotation along all the three pseudocubic axes, resulting in an isotropic structure of LSMO [43]. Given the anisotropic structure of the NGO single crystal, the NGO$(110)_{Or}$ and NGO$(001)_{Or}$ substrates have distinct effects on the LSMO films due to anisotropic strain and interfacial octahedral coupling [Figs. 1(a), 1(c), and 1(d)]. LSMO films with thickness ranging from 11 to 120 nm were simultaneously deposited on $(110)_{Or}$- and $(001)_{Or}$-oriented NGO substrates. The epitaxial conditions were examined with *in situ* reflection high-energy electron diffraction and *ex situ* HR-XRD measurements, showing the high quality of all LSMO films with atomically flat interfaces/surfaces (see Fig. S2 of the Supplemental Material [35]).

Reciprocal space mapping (RSM) was measured around the $(103)_{PC}$ and $(113)_{PC}$ reflections of the $(110)_{Or}$- and $(001)_{Or}$-oriented films by azimuthally rotating the samples by $90°$ with respect to the surface's normal (Fig. 2). The same Q_X values of the $(110)_{Or}$-oriented LSMO films and substrates confirm that the LSMO films are coherently grown on the NGO substrates with various orientations. The Q_X values of the $(113)_{PC}$ and $(\bar{1}\bar{1}3)_{PC}$ peaks measured from the $(001)_{Or}$-oriented LSMO films are found to show slight deviations relative to those of the substrates. We consider that these deviations do not derive from strain relaxation; the films still retain the coherent epitaxial growth. A systematic explanation of the horizontal deviations will be given in the following sections. More strikingly, different diffraction patterns in RSMs of these LSMO films are produced only via engineering a single crystallographic orientation of the NGO substrate with anisotropic structure. The reflections of the $(110)_{Or}$-oriented LSMO film present a central peak and two symmetric satellite peaks, while the reflections of the $(001)_{Or}$-oriented film split into two peaks.

Next, we present an analysis of the domain structures in LSMO films on the basis of the structural results. For the $(110)_{Or}$-oriented LSMO film, the two satellite peaks [indicated by red arrows in Fig. 2(a)] only appear in the RSMs for the $(03\bar{1})_{PC}$ and $(031)_{PC}$ reflections, whereas the $(\bar{1}30)_{PC}$ and $(130)_{PC}$ reflections do not possess these satellite peaks. This
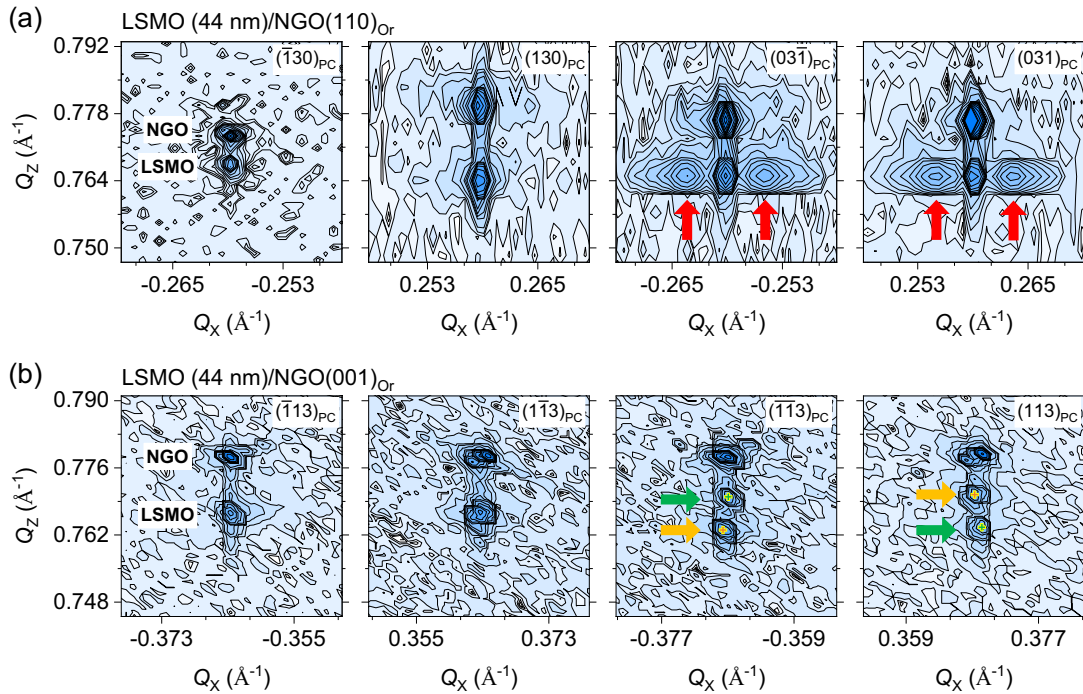
FIG. 2. RSMs of LSMO films. RSMs measured from the LSMO films grown on (a) NGO(110)$_{Or}$ and (b) NGO(001)$_{Or}$ substrates with the thickness of 44 nm. Totally distinct diffraction patterns are observed in the RSMs of the two oriented LSMO films. For the (110)$_{Or}$-oriented film, two additional satellite reflections at the same Q_X are shown for (031)$_{PC}$ and (03$\bar{1}$)$_{PC}$ reflections but absent for (130)$_{PC}$ and ($\bar{1}$30)$_{PC}$ reflections, as indicated by the red arrows. For the (001)$_{Or}$-oriented film, the (113)$_{PC}$ and ($\bar{1}\bar{1}$3)$_{PC}$ reflections split into two peaks, while the peak splitting disappears for the (1$\bar{1}$3)$_{PC}$ and ($\bar{1}$13)$_{PC}$ reflections, indicated by the orange and green arrows. Note that horizontal shifts of the (113)$_{PC}$ and ($\bar{1}\bar{1}$3)$_{PC}$ peaks are also observed as highlighted by the orange and green plus signs.

observation demonstrates that the structural domain is unidirectional. Rocking curve scans around the LSMO (020)$_{PC}$ reflection are shown as a function of the in-plane rotation angle (φ) (see Fig. S3(a) of the Supplemental Material [35]). A sinelike modulation of the individual satellite peak position is observed, further confirming the highly anisotropic nature of the structural domain. We also measured the rocking curve scans around the (0K0)$_{PC}$ reflections with K = 1, 2, 3, and 4 (see Fig. S3(b) of the Supplemental Material [35]). The satellite peaks are observed in all the rocking curves and their positions do not shift with K, implying that the satellites originate from the long-range modulations, which are periodic along the in-plane direction [7]. Along these lines, the satellite peaks observed in the RSMs are attributed to the unidirectional structural modulations along the in-plane [001]$_{PC}$ axis. In addition, only ($\bar{1}$30)$_{PC}$ and (130)$_{PC}$ reflections are observed to possess different Q_Z values, while (03$\bar{1}$)$_{PC}$ and (031)$_{PC}$ reflections share identical Q_Z values. This result suggests that the pseudocubic unit cells are all tilted only along the in-plane [100]$_{PC}$ direction. However, the long-range structural modulation only exists along the [001]$_{PC}$ direction, unambiguously signifying the monodomain structure in the (110)$_{Or}$-oriented LSMO films (see Fig. S4 of the Supplemental Material [35]). In specific, the long-range structural modulation does not originate from the twinned domain as observed in the LSMO/LSAT system [8]. Instead, the periodic displacements of the unit cells along the out-of-plane [010]$_{PC}$ direction, which are periodic along the in-plane [001]$_{PC}$ direction, should be responsible for the unidirectional structural

modulation [Fig. 3(a)]. Moreover, by calculating the satellite spacing (ΔQ_X) between the central reflection and satellite peaks, we can determine the periodicity ($\Lambda = 1/\Delta Q_X$) of the unidirectional lattice modulation to be ~24 nm [Fig. 3(a)]. The asymmetric ($\bar{1}$30)$_{PC}$ and (130)$_{PC}$ reflections and symmetric (03$\bar{1}$)$_{PC}$ and (031)$_{PC}$ reflections of the LSMO film further indicate that the LSMO film possesses an orthorhombic unit cell with (110)$_{Or}$ out-of-plane orientation (1$\bar{1}$0)$_{Or}$ and (001)$_{Or}$ in-plane orientations. This result is consistent with the previous observation obtained from the LSMO/NGO(110)$_{Or}$ system [41].

Unexpectedly, dissimilar reflection patterns are obtained when the orientation of the NGO substrates changes from (110)$_{Or}$ to (001)$_{Or}$. Under the influence of the NGO(001)$_{Or}$ substrate, the reflections of the LSMO film split into two peaks, rather than the satellite peaks observed in the (110)$_{Or}$-oriented film. The peak splitting of the reflections is ascribed to the twinned domains, which has been reported in other oxide ferroelastic systems [44,45]. The peak-splitting phenomenon is only detected for ($\bar{1}\bar{1}$3)$_{PC}$ and (113)$_{PC}$ reflections, but absent for (1$\bar{1}$3)$_{PC}$ and ($\bar{1}$13)$_{PC}$ reflections [Fig. 2(b)]. This observation demonstrates that the twinned domain formed in the (001)$_{Or}$-oriented LSMO film is also highly anisotropic. To better understand the domain structure, RSMs around the (103)$_{PC}$ and (013)$_{PC}$ reflections were also performed (see Fig. S5 of the Supplemental Material [35]). Peak splitting occurs in both the (103)$_{PC}$- and (013)$_{PC}$-diffraction conditions. However, the degree of the peak splitting (ΔQ_Z = 0.0032 Å) is smaller than that (ΔQ_Z = 0.0067 Å) observed
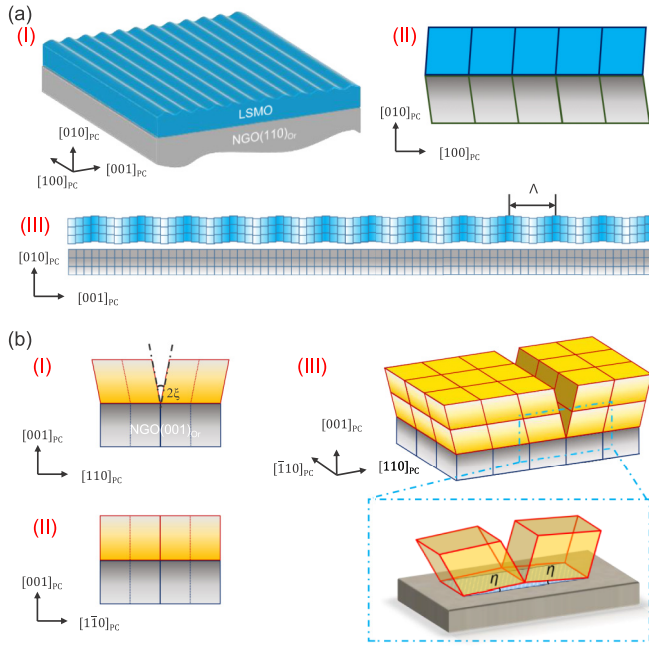
FIG. 3. Domain structures in LSMO films. (a) Schematic drawing of the unidirectional lattice modulation in LSMO/NGO(110)$_{Or}$ films. (I) The perspective view and side views along (II) [001]$_{PC}$ and (III) [100]$_{PC}$ of the lattice modulation. (b) Schematic illustrations of the unidirectional twinned domain in LSMO/NGO(001)$_{Or}$ films, including the side views along (I) [1$\bar{1}$0]$_{PC}$ and (II) [110]$_{PC}$ axes, as well as (III) the perspective view. The inset of (III) shows the zoomed-in view of the interface between the LSMO film and NGO substrate. Note that the (001)$_{PC}$ plane of LSMO film tilts away from the (001)$_{PC}$ plane of the NGO(001)$_{Or}$ substrate with a tilt angle of η.

in ($\bar{1}\bar{1}$3)$_{PC}$- and (113)$_{PC}$-diffraction conditions. These RSM features can be well explained by twinned domains formed along the in-plane [110]$_{PC}$ axis with the domain walls along the [1$\bar{1}$0]$_{PC}$ axis. Figure 3(b) shows the schematic illustrations of the twinned-domain structure, including the side and perspective views. In this domain configuration, the domains tilt their (110)$_{PC}$ planes oppositely by an angle ξ, causing the peak splitting at ($\bar{1}\bar{1}$3)$_{PC}$ and (113)$_{PC}$ reflections [Fig. 3(b)]. The oppositely tilting (110)$_{PC}$ planes can be decomposed into oppositely tilting planes with the tilting angle less than ξ along the [100]$_{PC}$ and [010]$_{PC}$ axes. This is the reason why the peak-splitting phenomenon with a smaller splitting degree appears for (103)$_{PC}$ and (013)$_{PC}$ reflections (see Fig. S5(b) of the Supplemental Material [35]). The film can be well described by a monoclinic structure with the in-plane axes a_m//[110]$_{PC}$ and b_m//[1$\bar{1}$0]$_{PC}$, the out-of-plane axis c_m//[001]$_{PC}$, and the monoclinic angle $\psi = 90° - \xi$, as schematically shown in Fig. 3(b)(III). The peak splitting at ($\bar{1}\bar{1}$3)$_{PC}$ and (113)$_{PC}$ reflections can be used to characterize the tilting angle of (110)$_{PC}$ plane [$\xi = \arctan(\Delta Q_Z/2Q_X)$] to be $\sim 0.53°$ [Fig. 3(b)].

Moreover, it is observed that the upper ($\bar{1}\bar{1}$3)$_{PC}$ peak shifts towards right and the lower ($\bar{1}\bar{1}$3)$_{PC}$ peak shifts towards left, whereas the case in (113)$_{PC}$ reflections is opposite, as indicated by the green and orange arrows in Fig. 2(b), These horizontal shifts indicate that the (001)$_{PC}$ plane of LSMO

tilts away from the (001)$_{PC}$ plane of NGO(001)$_{Or}$ substrate, forming an inclined angle η between LSMO(001)$_{PC}$ and NGO(001)$_{PC}$ planes as schematically shown in the inset of Fig. 3(b)(III) and Fig. S6 of the Supplemental Material [35]. The tilting angle ξ concomitant with the inclined angle η gives rise to the diffraction patterns in Fig. 2(b) (for details, see Fig. S7 of the Supplemental Material [35]).

The domain structures in LSMO films grown on NGO(110)$_{Or}$ and NGO(001)$_{Or}$ substrates demonstrate the crucial roles of anisotropic strain and interfacial octahedral coupling in determining the domain structure in ferroelastic oxide films.

B. Origin of the distinct domain structures formed in LSMO films via engineering the crystallographic orientation of NGO substrates

Formation of structural domains in ferroelastic films is well known to be caused by shear strain [7,8,36]. In our case, both the LSMO/NGO(110)$_{Or}$ and LSMO/NGO(001)$_{Or}$ systems contain the angle mismatch between films and substrates giving rise to the shear strain. Accordingly, the shear strain should be the primary motivation for the formation of the structural domains in the LSMO films. In the following, we will mainly discuss the formation of distinct domain structures in LSMO films grown on NGO(110)$_{Or}$ and NGO(001)$_{Or}$ substrates, in terms of anisotropic strain and interfacial octahedral proximity effect.

The ABO_3 perovskite structure is generally depicted utilizing the Glazer notation [46]. For example, the $a^- a^- c^+$ Glazer notation is corresponding to the orthorhombic structure. To clearly describe the domain structures and investigate the influence of interfacial octahedral coupling on domain structure and symmetry in the LSMO/NGO system, a more precise description of the rotations of each octahedron [47] is used here. In this description, a network of rotation signs of the individual octahedra is exploited to represent the OOR in a perovskite structure. In this definition, the clockwise and counterclockwise rotations of the individual octahedra along specific crystal axes are denoted as positive (+) and negative (−), respectively, and no rotation as zero (0), as illustrated in Fig. 4(a). The rotation signs of an octahedron are strictly restricted by two octahedral connectivity rules: (1) adjacent octahedra residing in a plane normal to a tilt axis should possess the opposite rotation signs about the axis; (2) the rotation signs of adjacent octahedra along the tilt axis should follow the in-phase or out-of-phase rotation designated in Glazer notation. As a result, the OOR of an octahedron can be deduced by that of the adjacent octahedron. The OOR in a perovskite structure can be visualized by drawing a rotation signs network of eight octahedra from a unit cell, in which the rotation signs of a specific octahedron fully determine the whole network. For consistency, here the rotation signs of the octahedron at the origin, i.e., the back bottom-left octahedron which is highlighted by the red circle, is used to represent the whole rotation network (Fig. 4). For example, the rotation signs network in Fig. 4(a) can be represented by [− − −].

For simplicity, we mainly focus on the rotation direction of the oxygen octahedra and ignore the relative difference
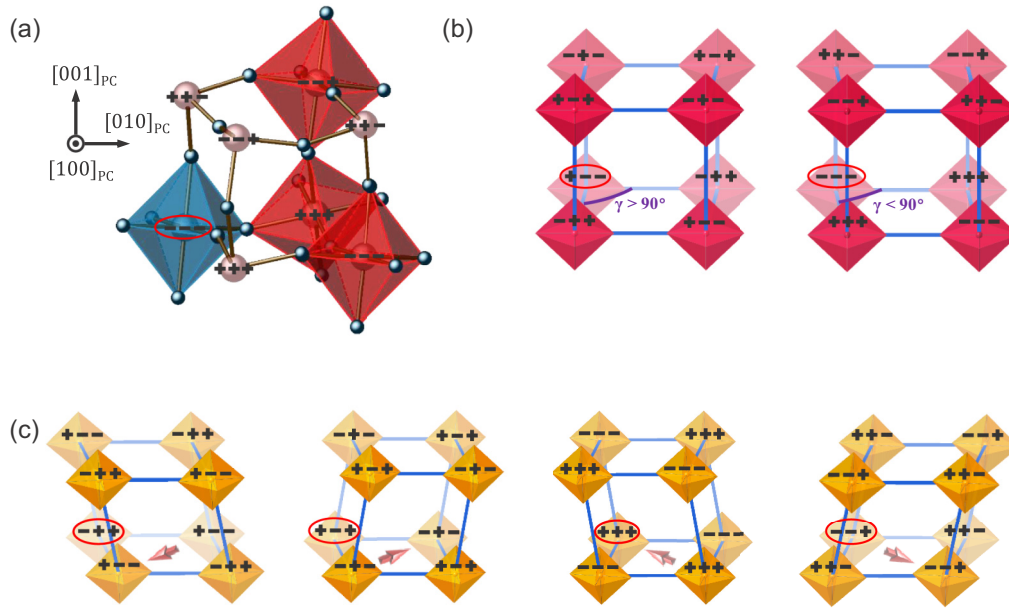
FIG. 4. OOR signs network in perovskite structure. (a) The definition of the rotation signs of an individual octahedron in a perovskite unit cell with clockwise $(+)$ and anticlockwise $(-)$. (b) Two oxygen octahedral rotation signs networks of the orthorhombic structure with the $a^-a^-a^+$ pattern, $[+--]_{Or}$ and $[---]_{Or}$ corresponding to $\gamma > 0$ and $\gamma < 0$, respectively. (c) Four OOR signs networks of the rhombohedral structure with the $a^-a^-a^-$ pattern, $[-++]_{Rh}$, $[+-+]_{Rh}$, $[+++]_{Rh}$, and $[--+]_{Rh}$. In these four OOR networks, the out-of-plane axes tilt along in-plane $[1\bar{1}0]_{PC}$, $[\bar{1}10]_{PC}$, $[\bar{1}\bar{1}0]_{PC}$, and $[110]_{PC}$ directions, respectively, as indicated by the solid arrows.

in the magnitude of the rotation. In this regard, the orthorhombic structure with $a^-a^-c^+$ Glazer notation can be simplified to $a^-a^-a^+$. Controlled by the two octahedral connectivity rules, the $a^-a^-c^+$ Glazer notation can be denoted by two rotation signs networks, i.e., the $[+--]_{Or}$ and the $[---]_{Or}$ networks, corresponding to the two orthorhombic structural domains with lattice angles γ and $180-\gamma$, respectively, which are the angles between $[100]_{PC}$ and $[010]_{PC}$ axes. For the NGO substrate, the $[+--]_{Or}$ and $[---]_{Or}$ sign networks correspond to $\gamma > 90°$ and $\gamma < 90°$, respectively (see Fig. 4(b) and Fig. S8 of the Supplemental Material [35]). Given the relationship between the orthorhombic axes and pseudocubic axes in this paper, the lattice angle γ of the NGO substrate should be greater than $90°$; the $[+--]_{Or}$ rotation signs network therefore is utilized to represent the orthorhombic NGO substrate. Actually, in perovskite materials with an orthorhombic structure, the value of the lattice angle γ is closely correlated with the orthorhombic lattice parameters. For the orthorhombic structure with $a_{Or} < b_{Or}$, such as NGO, CaRuO$_3$, and SmFeO$_3$, the $[+--]_{Or}$ rotation signs network corresponds to $\gamma > 90°$, while for the orthorhombic structure with $a_{Or} > b_{Or}$, such as La$_{0.67}$Ca$_{0.33}$MnO$_3$ (LCMO), SrRuO$_3$, and LaGaO$_3$, the $[+--]_{PC}$ rotation signs network corresponds to $\gamma < 90°$. The $a^-a^-a^-$ Glazer notation can be represented by four rotation signs networks, namely, $[-++]_{Rh}$, $[+-+]_{Rh}$, $[+++]_{Rh}$, and $[--+]_{Rh}$ rotation signs networks, which correspond to the four rhombohedral structural domains (see Fig. 4(c) and Fig. S9 of the Supplemental Material [35]). For bulk LSMO, the above four rhombohedral structure domains are derived from the undistorted cubic structure by compression of the four body diagonal directions, leading to the tilting pseudocubic unit

cells along $[1\bar{1}0]_{PC}$, $[\bar{1}10]_{PC}$, $[\bar{1}\bar{1}0]_{PC}$, and $[110]_{PC}$ directions, as indicated by the solid arrows in Fig. 4(c).

The symmetry mismatch between a substrate and an epitaxial film can alter the crystallographic symmetry of the film, resulting from the structural couplings at the heterointerface [28,47,48]. As observed in LSMO/NGO(110)$_{Or}$ system, LSMO films with orthorhombic structure $(a^-b^-c^+)$ are formed by heterostructuring with orthorhombic NGO(110)$_{Or}$ substrate. The opposite tilting directions of the asymmetric $(\bar{1}30)_{PC}$ and $(130)_{PC}$ reflections for the film and substrate demonstrate that the $[+--]_{Or}$ rotation signs network of the orthorhombic LSMO film corresponds to $\gamma < 90°$, resembling the case in LCMO. However, the LSMO film grown on NGO(001)$_{Or}$ exhibits a monoclinic structure with $a^-a^-c^-$ Glazer notation. Obviously, the NGO(110)$_{Or}$ substrate shows a stronger effect in modifying the OOR in LSMO film in comparison to the NGO(001)$_{Or}$ substrate. This can be attributed to the larger in-plane OOR mismatch between the LSMO film and NGO(110)$_{Or}$ substrate by contrast with that between the LSMO film and NGO(001)$_{Or}$ substrate.

Identical to the cases in all-orthorhombic (110)$_{Or}$-oriented epitaxial systems [47], in LSMO/NGO(110)$_{Or}$ films, there are two possible interfacial structures: $[---]_{Or}/[+--]_{Or}$ and $[+--]_{Or}/[+--]_{Or}$, where the left rotation signs network corresponds to the LSMO film, and the right rotation signs network corresponds to the NGO substrate, as schematically shown in Fig. 5(a). Considering the fact that the $[+--]_{Or}$ and $[---]_{Or}$ rotation signs networks share the same in-plane lattice parameters, the lattice mismatches in $[---]_{Or}/[+--]_{Or}$ and $[+--]_{Or}/[+--]_{Or}$ configurations are identical. The strain effect should play the same roles in these two configurations. However, completely different
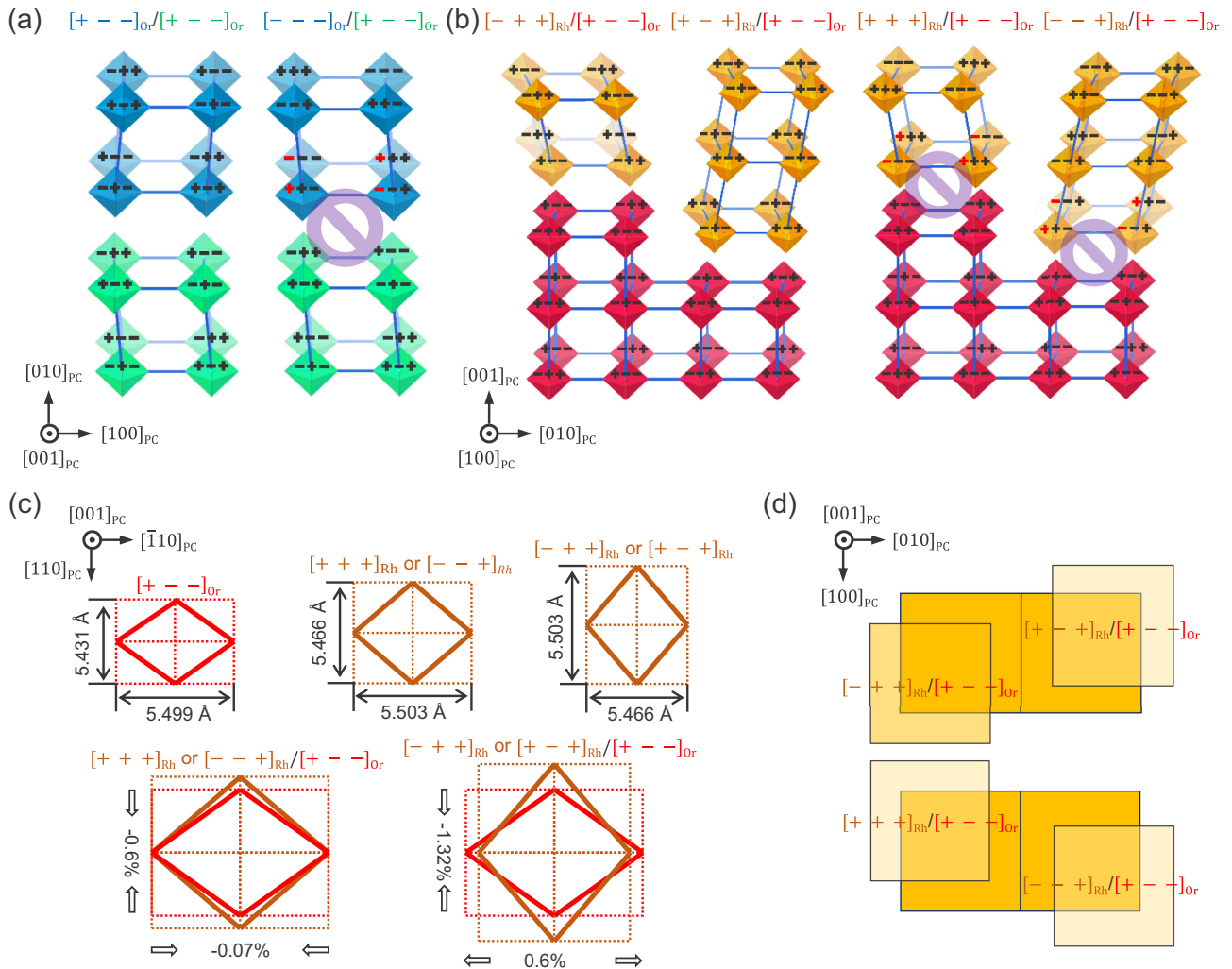
FIG. 5. Interfacial OOR- and strain-dependent domain structure in LSMO films on NGO(110)$_{Or}$ and NGO(001)$_{Or}$ substrates. (a) Rotation signs networks across LSMO/NGO(110)$_{Or}$ interfaces. The left and right panels show the $[+--]_{Or}/[+--]_{Or}$ and $[---]_{Or}/[+--]_{Or}$ configurations, respectively. To ensure the octahedral connectivity at the interface, the left configuration is energetically favored. (b) Rotation signs networks across LSMO/NGO(001)$_{Or}$ interfaces, including $[-++]_{Rh}/[+--]_{Or}$, $[+-+]_{Rh}/[+--]_{Or}$, $[+++]_{Rh}/[+--]_{Or}$, and $[--+]_{Rh}/[+--]_{Or}$. (c) Strain states in LSMO/NGO(001)$_{Or}$ films with different rotation signs networks. (d) Structural domains corresponding to the four rotation signs networks shown in (b). From the perspective of interfacial octahedral connectivity, only the $[-++]_{Rh}/[+--]_{Or}$ and $[+--]_{Rh}/[+--]_{Or}$ interfacial octahedral connectivities are allowed, forming the structural domains in the top panel, while from the perspective of epitaxial strain, the $[+++]_{Rh}/[+--]_{Or}$ and $[--+]_{Rh}/[+--]_{Or}$ interfacial octahedral connectivities are energetically favored, forming the structural domains in the bottom panel.

octahedral connectivity is found at $[---]_{Or}/[+--]_{Or}$ and $[+--]_{Or}/[+--]_{Or}$ heterointerfaces. The $a^-a^-a^+$ rotation pattern is retained at the interface of $[+--]_{Or}/[+--]_{Or}$, while the $[---]_{Or}/[+--]_{Or}$ interface violates the two octahedral connectivity rules mentioned above. All the unmatched rotation signs at the $[---]_{Or}/[+--]_{Or}$ interface are highlighted by red signs in the right panel of Fig. 5(a). Owing to the less unmatched rotation signs at $[+--]_{Or}/[+--]_{Or}$ interface compared to the $[---]_{Or}/[+--]_{Or}$ interface, the former is more energetically favored to maintain the interfacial octahedral connectivity. Therefore, the LSMO film grown on NGO(110)$_{Or}$ substrate is inclined to form single-domain structure other than the twinned structure in LSMO/STO and LSMO/LSAT systems [7,8]. To relieve the shear strain originating from the

angle mismatch between the film and substrate, the long-range lattice modulation emerges in the LSMO film. The anisotropic strain received from the orthorhombic NGO(110)$_{Or}$ substrate should be the reason for the formation of the periodic lattice modulation only along the [110]$_{PC}$ direction, instead of both the two orthogonal directions.

The above analysis method is not limited to the (110)$_{Or}$-oriented films. We now proceed to discuss the origin of the domain structure formed in LSMO films grown on NGO(001)$_{Or}$ substrates. As aforementioned, the (001)$_{Or}$-oriented LSMO film presents a monoclinic structure with the $a^-a^-c^-$ Glazer notation, which can be simplified to be $a^-a^-a^-$ via disregarding the magnitude of the OOR. The $a^-a^-a^-$ Glazer has four rotation signs networks, involving $[-++]_{Rh}$, $[+-+]_{Rh}$, $[+++]_{Rh}$, and $[--+]_{Rh}$ networks.

When LSMO film is grown on NGO(001)$_{Or}$ substrate, four possible structures exist at LSMO/NGO(001)$_{Or}$ interfaces, i.e., $[-++]_{Rh}/[+--]_{Or}$, $[+-+]_{Rh}/[+--]_{Or}$, $[+++]_{Rh}/[+--]_{Or}$, and $[--+]_{Rh}/[+--]_{Or}$, as illustrated in Fig. 5(b). Unlike the situation in LSMO/NGO(110)$_{Or}$ system where the strain effect cannot distinguish the two rotation signs networks of the LSMO film and the domain structure is solely controlled by the interfacial octahedral connectivity, in LSMO/NGO(001)$_{Or}$ system the $[-++]_{Rh}$, $[+-+]_{Rh}$, $[+++]_{Rh}$, and $[--+]_{Rh}$ rotation signs networks possess different lattice mismatches with the substrate. The domain structure in the LSMO film results from the competition and cooperation between the strain effect and the interfacial octahedral connectivity.

In the aforementioned four structures existing in LSMO/NGO(001)$_{Or}$ system, distinct interfaces are observed. $[-++]_{Rh}/[+--]_{Or}$ and $[+-+]_{Rh}/[+--]_{Or}$ interfaces maintain the $a^-a^-a^-$ rotation across the interfaces, while $[+++]_{Rh}/[+--]_{Or}$, and $[--+]_{Rh}/[+--]_{Or}$ interfaces have mismatched rotation signs at the interfaces, as indicated by the red signs in the right panel of Fig. 5(b). In this perspective, the LSMO/NGO(001)$_{Or}$ interface energetically favors the former two structures over the latter two structures. The $[-++]_{Rh}$ and $[+-+]_{Rh}$ rotation signs networks correspond to the rhombohedral structure domains with the pseudocubic unit cells tilting along the $[1\bar{1}0]_{PC}$ and $[\bar{1}10]_{PC}$ axes as shown in the top panel of Fig. 5(d). On the other hand, the NGO(001)$_{Or}$ substrate can provide different anisotropic strain to the four rotation signs networks, i.e., $[-++]_{Rh}$, $[+-+]_{Rh}$, $[+++]_{Rh}$, and $[--+]_{Rh}$.

To reveal the influence of the strain effect on the structural domains in LSMO/NGO(001)$_{Or}$ film, the strain states in the four rotation signs networks are analyzed. Figure 5(c) shows the strain states in $[-++]_{Rh}$, $[+-+]_{Rh}$, $[+++]_{Rh}$, and $[--+]_{Rh}$ rotation signs networks grown on NGO(001)$_{Or}$ substrate. For clarity, we mainly focus on the strain states along the $[110]_{PC}$ and $[\bar{1}10]_{PC}$ axes, i.e., $[100]_{Or}$ and $[010]_{Or}$ axes of the NGO substrate, which are perpendicular to each other. When the LSMO film with $[+++]_{Rh}$ or $[--+]_{Rh}$ network is grown on NGO(001)$_{Or}$ substrate, the film bears in-plane anisotropic strain, -0.6% along the $[110]_{PC}$ axis and -0.07% along the $[\bar{1}10]_{PC}$ axis. If the film is manifested as $[-++]_{Rh}$ or $[+-+]_{Rh}$ network, the anisotropic strain is prominently altered to be -1.32% along the $[110]_{PC}$ axis and 0.6% along the $[\bar{1}10]_{PC}$ axis. The epitaxial strain imposed on the $[-++]_{Rh}$ and $[+-+]_{Rh}$ networks is appreciably larger than that imposed on the $[+++]_{Rh}$ and $[--+]_{Rh}$ networks along both the $[110]_{PC}$ and $[\bar{1}10]_{PC}$ axes. In this perspective, to lower the system energy, the LSMO/NGO(001)$_{Or}$ system tends to form $[+++]_{Rh}/[+--]_{Or}$ and $[--+]_{Rh}/[+--]_{Or}$ structures where the film experiences minor strain. Accordingly, the twinned domains with the pseudocubic unit cells tilting along the $[110]_{PC}$ and $[\bar{1}10]_{PC}$ directions are formed in the LSMO film, as shown in the bottom panel of Fig. 5(d). To ensure the interfacial octahedral connectivity and minimize the epitaxial strain imposed on the film, the twinned domains in the LSMO film that tend to form are different. In other words, the structural domains in the LSMO film are manipulated by competition between the interfacial octahedral connectivity

and strain effect. The observed twinned domains along the in-plane $[110]_{PC}$ direction demonstrate that the strain effect plays a dominant role in determining the domain structure in LSMO films grown on NGO(001)$_{Or}$ substrate.

So far, we have explained why entirely different domain structures are formed in LSMO films only via engineering a single crystallographic orientation of the NGO substrate with a large structural anisotropy from the point of view of the interfacial octahedral connectivity and anisotropic strain. In the LSMO film grown on NGO(110)$_{Or}$ substrate, due to the indistinguishable strain effect of different structural domains, a monodomain structure is maintained due to the unique octahedral connectivity at the heterointerfaces. The collective effect of shear strain and anisotropic strain prompts the formation of the unidirectional lattice modulation. In contrast, for the LSMO/NGO(001)$_{Or}$ epitaxial system, the large difference between the magnitudes of the anisotropic strain in various structural domains facilitates the formation of twinned domains that suffer minor strain, even at the expense of the interfacial octahedral connectivity. Furthermore, our results also provide strong evidence that a large anisotropic strain in an epitaxial film is capable to reorient the crystallographic axes of the film, ensuring the minimal strain states in the film. This observation will shed light on the investigation of the coupling between the epitaxial strain and OOR in an epitaxial film, especially those with out-of-phase rotations about both the two in-plane axes, such as the rhombohedral ($a^-a^-a^-$) and (001)$_{Or}$-oriented orthorhombic ($a^-a^-c^+$) films.

C. Magnetic anisotropy and orbital occupancy in LSMO films grown on NGO substrates

Apart from the 44-nm-thick LSMO films, RSMs were also performed on other LSMO films with t_{LSMO} ranging from 11 to 120 nm, where t_{LSMO} stands for the thickness of LSMO films (see Figs. S10 and S11 of the Supplemental Material [35]). The unidirectional lattice modulation and twinned domains are observed in all the (110)$_{Or}$- and (001)$_{Or}$-oriented LSMO films thicker than 22 nm, whereas the films with $t_{LSMO} = 11$ nm show single-domain structures reflected by the disappeared satellite peaks and split peaks in the RSMs measured from the (110)$_{Or}$- and (001)$_{Or}$-oriented LSMO films, respectively. This result attests that there is a critical thickness between 11 and 22 nm beyond which the unidirectional lattice modulation and twinned domains emerge in LSMO films. The formation of the structural domains is controlled by the total elastic energy E. If the elastic behavior of the film is approximated as isotropic, the total elastic energy E in a strained film is given by

$$E = \left[\frac{1}{2}G\gamma^2 + 2G\frac{1+v}{1-v}\varepsilon^2\right]V,$$

where G, v, γ, ε, and V are the shear modulus, Poisson's ratio, shear-angle mismatch, in-plane lattice mismatch, and volume of the film, respectively [44]. It is clear that the energy per unit area of the film increases linearly with film thickness. The elastic energy of the ferroelastic film can be reduced by the formation of appropriate lattice defects, such as the lattice modulation and twinned domains. In this case, E increases linearly with increasing t_{LSMO}. When t_{LSMO} reaches the critical
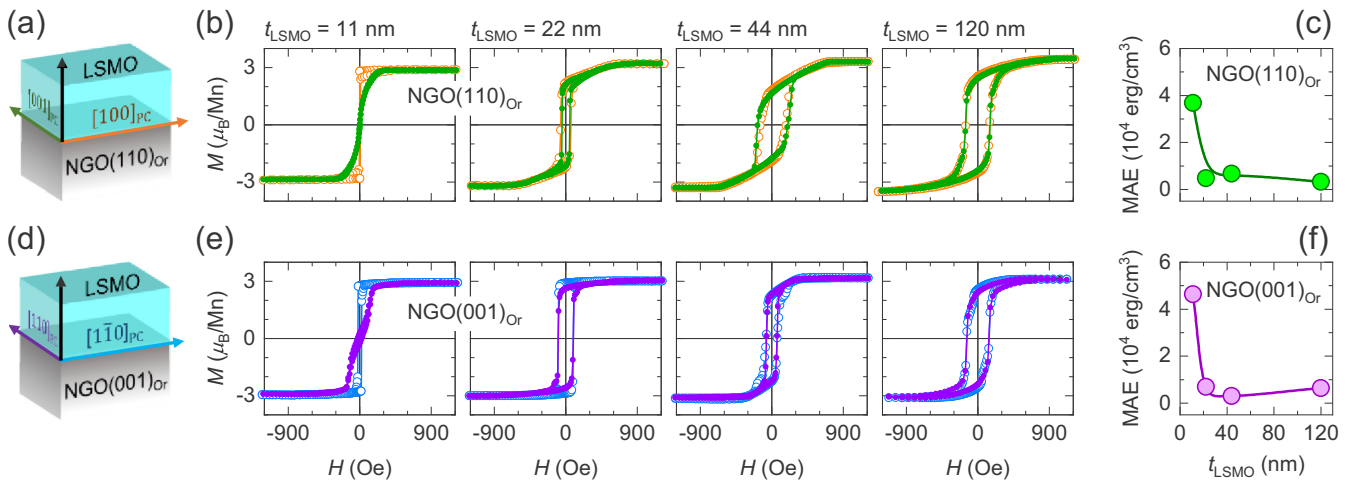
FIG. 6. Magnetic anisotropy of LSMO/NGO films with different domain structures. (a), (d) Schematic illustrations of the LSMO films grown on $NGO(110)_{Or}$ and $NGO(001)_{Or}$ substrates with the in-plane axes denoted. (b), (e) Magnetic hysteresis loops (M-H curves) measured at 100 K from the above $LSMO/NGO(110)_{Or}$ and $LSMO/NGO(001)_{Or}$ films with the applied field along the in-plane axes which are perpendicular with respect to each other, as indicated by the arrows in (a), (d). The strong paramagnetic background from the NGO substrates is subtracted. (c), (f) The corresponding magnetic anisotropy energy extracted from the M-H curves.

thickness, the lattice modulation and twinned domains appear, accompanied with a rearrangement of the LSMO lattices, and E is reduced.

To explore the correlation between the magnetic properties and structural distortion in LSMO films, the magnetic hysteresis behaviors of the LSMO films are investigated (Fig. 6). During the measurements, magnetic field H was applied either perpendicular or parallel to the unidirectional lattice modulation/twinned domains for the $(110)_{Or}/(001)_{Or}$-oriented LSMO films, as indicated by the arrows in Fig. 6(a)–6(d). By comparing the magnetic switching behaviors measured along the two orthogonal directions, the in-plane magnetic anisotropy energy (MAE) is estimated (see Fig. S12 of the Supplemental Material [35]). The MAE extracted from the magnetic hysteresis loops [M-H curves, Figs. 6(b) and 6(e)] measured from the LSMO films grown on $NGO(110)_{Or}$ and $NGO(001)_{Or}$ substrates is, respectively, plotted in Figs. 6(c) and 6(f) as a function of t_{LSMO}. For the $(110)_{Or}$-oriented LSMO films, the MAE of the 11-nm-thick film is 3.69×10^4 erg cm^{-3}, and the LSMO films exhibit a dramatic decay of MAE to 4.8×10^3 erg cm^{-3} as t_{LSMO} increases to 22 nm. Further increasing t_{LSMO} to 44 nm and then to 120 nm does not significantly change the MAE [Fig. 6(c)]. Similarly, for the $(001)_{Or}$-oriented LSMO films, as t_{LSMO} increases from 11 to 22 nm, the MAE also promptly decreases from the maximum value of 4.64×10^4 erg cm^{-3} to 6.88×10^3 erg cm^{-3}. It then stabilizes and remains at this level as t_{LSMO} increases to 44 and 120 nm [Fig. 6(f)]. The similar tendencies of the t_{LSMO}-dependent MAE suggest that the same physical mechanisms exist to determine the MAE of $(110)_{Or}$- and $(001)_{Or}$-oriented LSMO films, and the formation of the unidirectional lattice modulation and twinned domains should play essential roles.

Now, we explain how the changes of t_{LSMO} tune the MAE of LSMO films in such a manner. Developing strategies to engineer the magnetic anisotropy of ferromagnetic oxide heterostructures is pivotal to uncover exotic phenomena and pave the path towards novel practical logic or memory devices. Interfacial octahedral coupling [48–50], epitaxial stain [51,52], spin-orbital coupling [53,54], and ferroelectric polarization [55] are several well-known strategies. Taking $La_{1−x}Sr_xMn O_3$ as an example, upon controlling the dimensionality of the $SrIrO_3$ (SIO) layer, a magnetic easy-axis reorientation is observed in LSMO/SIO superlattices, attributed to a spin-orbital coupling state with a relatively large orbital-dominated moment that develops in the typically paramagnetic SIO layer [53]. Similarly, an unexpected realignment of the magnetic easy axis in an ultrathin LSMO film is triggered via interfacial oxygen octahedral coupling-induced oxygen network modification, which alters the Mn–O-Mn bond angle θ, and thus the hybridization between Mn $3d$ and O $2p$ orbitals [48]. Nonetheless, when the effect of interfacial octahedral coupling, which possesses a short impact length scale of $\sim$2 nm, is attenuated in thick LSMO films, the magnetic anisotropy is verified to highly rely on the in-plane orbital occupancy, which is governed by the anisotropic strain [51]. The ferroelectric screening effect at the $PbZr_{0.2}Ti_{0.8}O_3/La_{0.8}Sr_{0.2}MnO_3$ interface also shows a crucial influence on the d-orbital occupancy of $La_{0.8}Sr_{0.2}MnO_3$ layer, and subsequently tuning the magnetic anisotropy [55].

In our pure LSMO films, the effects of spin-orbital coupling and ferroelectric polarization can be first excluded. In addition, since the minimum thickness of LSMO films here is 11 nm, which far exceeds the impact range of the interfacial octahedral coupling (length scale of $\sim$2 nm) [28,48], the interfacial octahedral coupling between LSMO and NGO should not be the key factor in determining the magnetic anisotropy in LSMO films. At first glance, one may consider that the suppressed in-plane magnetic anisotropy with increasing t_{LSMO} is related to the thickness effect of LSMO films, e.g., the ferromagnetic-metallicity degradation at the LSMO interface, which is referred to the "dead layer" effect. The metallicity degradation at the interface can weaken the $Mn_{3d} - O_{2p}$ orbital hybridization [56], and thus influence the magnetic anisotropy to some extent. Nevertheless, such a

thickness effect may not play a dominant role in determining the magnetic properties in the present case, since the thicknesses of LSMO films are far beyond the critical thickness (3–7 unit cells) of the dead layer effect [57,58], and metallic behaviors are maintained within the whole temperature range below the metal-insulator transition temperature (see Fig. S13 of the Supplemental Material [35]). To further clarify this issue, LSMO/STO bilayers were grown on NGO(110)$_{Or}$ and NGO(001)$_{Or}$ substrates (see Fig. S14 of the Supplemental Material [35]). The formation of the unidirectional lattice modulation and twinned domains is hindered by the insertion of the STO buffer layers (see Figs. S15(a) and S15(b) of the Supplemental Material [35]). In the meantime, both the (110)$_{Or}$- and (001)$_{Or}$-oriented LSMO films possess large MAE (see Figs. S15(c) and S15(d) of the Supplemental Material [35]). This result implies that the modulation of the MAE should be strongly correlated to the unidirectional lattice modulation and twinned domains formed in LSMO films, whereas the thickness effect only shows limited influence.

In fact, the shape effect of the domain structures has exhibited a significant impact on the magnetic anisotropy in LSMO films grown on cubic STO substrates with miscut angles, where the strain state is isotropic [40]. In this LSMO/STO system, since contributions of magnetocrystalline anisotropy and strain anisotropy along the in-plane two orthogonal directions are identical, the in-plane magnetic anisotropy is mainly controlled by the shape anisotropy of the domain structure [40]. However, in the present LSMO/NGO system with strong anisotropic strain, the shape effect of the unidirectional domain structure should not dominate the in-plane magnetic anisotropy. Moreover, if the in-plane magnetic anisotropy is governed by the shape effect of the domain structure, an enhanced in-plane magnetic anisotropy will be induced, which contradicts the experimental results.

For the (110)$_{Or}$- and (001)$_{Or}$-oriented LSMO films with $t_{LSMO} = 11$ nm, which retain the single-domain structures, the magnetic easy axis aligns along the axis with a relatively minor compressive strain or a relatively large tensile strain. The strain effect has demonstrated its great potential in tailoring the magnetic anisotropy of manganite films. For instance, strong in-plane uniaxial magnetic anisotropy is caused in LSMO/LaGaO$_3$ and LSMO/NGO epitaxial systems by the anisotropic strain imposed onto the LSMO films, exhibiting the same correlation between the strain states and magnetic easy-axis alignments as the present case [52,59]. Therefore, we consider that the strong uniaxial magnetic anisotropy in the 11-nm-thick LSMO films is attributed to the anisotropic strain. As t_{LSMO} increases, the unidirectional lattice modulation and twinned domains evoked anisotropic strain reliefs should account for the markedly suppressed in-plane magnetic anisotropy.

For the (110)$_{Or}$-oriented LSMO films, the 11-nm LSMO film suffers compressive strain from the orthorhombic NGO substrate along both the in-plane (100)$_{PC}$ and (001)$_{PC}$ axes with the strain along the (001)$_{PC}$ axis larger than that along the (100)$_{PC}$ axis, giving rise to the magnetic easy axis along the (100)$_{PC}$ axis. As t_{LSMO} is increased to 22 nm, the unidirectional lattice modulation along the (001)$_{PC}$ axis emerges from the film, leading to partial relief of the large compressive strain along the (001)$_{PC}$ axis. As a result, the anisotropy

of the epitaxial strain in the LSMO film is reduced, and therefore decreases the magnetic anisotropy, as shown in dramatically reduced MAE of the 22-nm LSMO film. Further increasing t_{LSMO} to 44 and 120 nm does not notably change the MAE. The magnetic properties of LSMO films with the thickness ranging from 22 to 120 nm are almost biaxially isotropic, reflected by the similar magnetic switching behaviors along [100]$_{PC}$ and [001]$_{PC}$ axes as well as the negligible MAE, signifying the prominent role of the unidirectional lattice modulation in tailoring the magnetic anisotropy of LSMO films. Identical to the case in (110)$_{Or}$-oriented LSMO films, the emergence of the unidirectional twinned domains in LSMO films with $t_{LSMO} \geqslant 22$ nm is capable to relieve the compressive strain along the corresponding axis, therefore reducing the MAE. Such an anisotropic strain relief has exhibited its nontrivial effect in tuning the magnetic anisotropy in other systems [60,61]. However, in these systems the anisotropic strain relief of the film mainly arises from the recovery of bulk state from the strained state, which is different from our present case.

To validate the anisotropic strain relief modulated in-plane magnetic anisotropy in LSMO/NGO system, the orbital occupancy of the Mn $3d$ electrons were characterized, which were proved to be profoundly sensitive to both magnetic anisotropy and epitaxial strain [51]. Element-specific XAS at the Mn $L_{2,3}$ edge is conducted using the out-of-plane (I_{out}) and in-plane (I_{in}) linearly polarized x-ray beams in the TEY mode. The details of the experimental configurations of XLD for the (110)$_{Or}$- and (001)$_{Or}$-oriented LSMO films are shown in Figs. S16(a) and S16(b) of the Supplemental Material [35]. One can anticipate that the absorption of x rays polarized along the out-of-plane direction (or in-plane direction) arises largely from the unoccupied Mn $d_{3z^2-r^2}$ (or $d_{x^2-y^2}$) orbitals, i.e., the holes [62,63]. By integrating the XLD ($I_{in}-I_{out}$) between 649 and 659 eV, the obtained area of XLD (ALD) directly reflects the orbital configuration of d electrons (see Fig. 7 and Fig. S16 of the Supplemental Material [35]) [62,64,65]. For the unstrained bulk LSMO, a degenerated orbital occupancy is expected; thus no XLD signal is observed. For strained LSMO thin films, while tensile strain favors the $d_{x^2-y^2}$ orbital occupancy, a compressive strain favors the $d_{3z^2-r^2}$ orbital occupancy, yielding negative and positive ALD, respectively [63,65]. In the present case, preferential $d_{3z^2-r^2}$ orbital occupancy with positive ALD is observed for all the LSMO films grown on NGO(110)$_{Or}$ and NGO(001)$_{Or}$ substrates under compressive strain (see Fig. 7 and Fig. S16 of the Supplemental Material [35]). The ALD of the 11-nm-thick LSMO films grown on NGO(110)$_{Or}$ and NGO(001)$_{Or}$ substrates are 1.22 and 1.14%, respectively, agreeing well with the previous study [66]. With increasing t_{LSMO} to 22 nm, both the (110)$_{Or}$- and (001)$_{Or}$-oriented LSMO films show steeply reduced ALD. While t_{LSMO} is further increased to 44 nm, the ALD of the LSMO films remains almost unchanged, displaying the same tendency as the MAE [Figs. 7(c) and 7(d)]. Since the orbital occupancy strongly depends on the strain states of LSMO films [65], the reduced ALD suggests the notably suppressed compressive strain in the 22- and 44-nm LSMO films. The lateral XLD result further confirms that the strain reliefs in the (110)$_{Or}$- and (001)$_{Or}$-oriented LSMO films mainly occur along the in-plane [001]$_{PC}$ and [110]$_{PC}$ axes, where the lattice
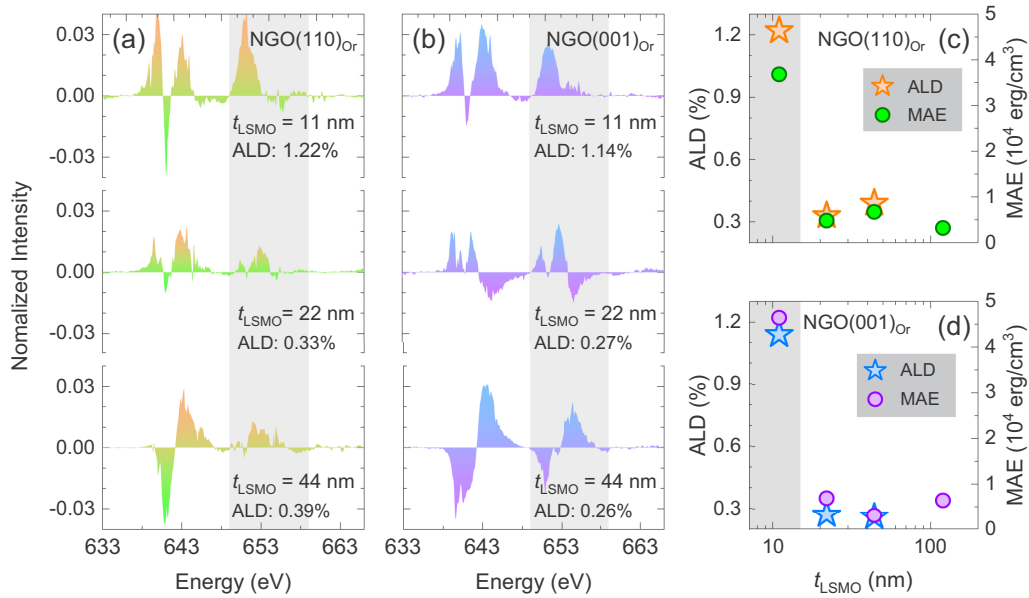
FIG. 7. Orbital occupancy probed by x-ray absorption spectroscopy. (a), (b) X-ray linear dichroism of Mn $L_{2,3}$ edge of LSMO films grown on NGO(110)$_{Or}$ and NGO(001)$_{Or}$ substrates, respectively. The integrating range for ALD is colored in gray. All XLDs were measured at 300 K. (c), (d) Integrated linear dichroism from 649–659 eV normalized by the ($I_{in} + I_{out}$) for LSMO films, ALD = ($I_{in} - I_{out}$)/($I_{in} + I_{out}$) × 100%. The corresponding MAE are also included for reference.

modulation and twinned domains exist (see Fig. S17 of the Supplemental Material [35]). These results suggest that the modulated in-plane magnetic anisotropy is intimately associated with the Mn 3d-orbital occupancy, which is governed by the unidirectional lattice modulation and twinned domains-induced anisotropic strain reliefs.

In addition to the crystal-field deformation-controlled Mn 3d-orbital occupancy as discussed above, the strain-mediated Mn$_{3d}$-O$_{2p}$ orbital hybridization is also required to be considered for the modulation of the in-plane magnetic anisotropy [48]. The Mn$_{3d}$-O$_{2p}$ orbital hybridization is characterized by the conduction bandwidth $\omega \approx \cos[(\pi - \theta)/2]/d^{3.5}$, where θ and d refer to the Mn–O–Mn bond angle and Mn–O bond length [67]. Both θ and d play vital roles in determining the Mn$_{3d}$-O$_{2p}$ orbital hybridization. First, we focus on the θ-dependent Mn$_{3d}$-O$_{2p}$ orbital hybridization. Density-functional calculations have revealed the ability of epitaxial strain to directly modify the magnitude of the octahedral rotations about different crystallographic directions [68,69]. However, both experimental and computational studies demonstrated that the in-plane Mn–O–Mn bond angles are weakly sensitive to the epitaxial strain state, instead; the elastic strain energy imposed on the film by the substrate is mainly accommodated by changes of the in-plane Mn–O bond lengths [68,70]. Since the in-plane magnetic anisotropy of LSMO films only depends on the in-plane Mn$_{3d}$-O$_{2p}$ orbital hybridization, the θ-dependent Mn$_{3d}$-O$_{2p}$ orbital hybridization should be ruled out for the observed in-plane magnetic anisotropy.

Then, we move our attention to the strain-driven Mn–O bond length and its effects on in-plane Mn$_{3d}$-O$_{2p}$ orbital hybridization and magnetic anisotropy in LSMO films. As described in a previous report [68], the in-plane bond lengths couple linearly to epitaxial strain. A large Mn–O bond length

leads to a weak Mn$_{3d}$-O$_{2p}$ orbital hybridization, while a short Mn–O bond length gives rise to a strong Mn$_{3d}$-O$_{2p}$ orbital hybridization. Anisotropic strain will yield an in-plane anisotropy of Mn–O bond lengths, and thus a resultant anisotropic Mn$_{3d}$-O$_{2p}$ orbital hybridization. Based on the analysis of the strain states in LSMO films [Fig. 1(a)], a relatively strong Mn$_{3d}$-O$_{2p}$ orbital hybridization arises along the in-plane [001]$_{PC}$ and [110]$_{PC}$ axes for (110)$_{Or}$- and (001)$_{Or}$-oriented LSMO films, respectively, facilitating magnetic easy axes along the identical axes [48]. This contradicts the results obtained from the magnetic measurements (Fig. 6), signifying that the strain-driven d-dependent Mn$_{3d}$-O$_{2p}$ orbital hybridization also shows negligible influence on the in-plane magnetic anisotropy of LSMO films.

One may have recognized that totally opposite effects of the strain-driven Mn–O bond lengths are devoted to the d-orbital occupancy and Mn$_{3d}$-O$_{2p}$ orbital hybridization. Namely, if the Mn–O bond length d is compressed along one specified axis, the Mn$_{3d}$-O$_{2p}$ orbital hybridization is strengthened by broadening the conduction bandwidth ω. Hence, the double-exchange governed ferromagnetic interaction is enhanced along the corresponding axis. However, such octahedral deformation that modifies the MnO$_6$ crystal field should lower the energy of the corresponding orbital state and enhance the orbital occupancy, leading to the weakened ferromagnetic interaction. The observed in-plane magnetic anisotropy indicates the dominant status of the strain-driven crystal-field effect in the competition with strain-driven Mn$_{3d}$-O$_{2p}$ orbital hybridization, agreeing well with a recent report [51].

By taking all these observations into account, we can reach a conclusion that the in-plane magnetic anisotropy of the LSMO films mainly originates from the anisotropic strain induced in-plane orbital occupancy preference. With increasing

t_{LSMO}, the anisotropic strain is relieved by the emerged lattice modulation and twinned domains in $(110)_{\text{Or}}$- and $(001)_{\text{Or}}$-oriented LSMO films, respectively, subsequently suppressing the anisotropy of the in-plane $d_{x^2-y^2}$ orbital occupancy as well as the in-plane magnetic anisotropy.

IV. CONCLUSION

In summary, by varying the crystallographic orientation of the NGO substrates from $(110)_{\text{Or}}$ to $(001)_{\text{Or}}$, the type of domain structure in LSMO films changes from unidirectional lattice modulation to unidirectional twinned domains, demonstrating that the domain structures in ferroelastic LSMO films are not only correlated to the shear strain but also the interfacial oxygen octahedral coupling as well as anisotropic strain. Engineering the unidirectional lattice modulation and twinned domains provides opportunities to tune the anisotropic strain, and to manipulate the orbital occupancy and magnetic anisotropy. Our results build a bridge linking the anisotropic strain-relief mechanism of domain structure to the electronic state and subsequent magnetic order in ferroelastic heterostructures. The manipulation of domain structure can be further extended to other perovskite oxide heterostructures with strong correlation between various ferroic orders for realizing potential oxide electronic devices with tunable functionalities.

[1] E.-J. Guo, R. Desautels, D. Keavney, M. A. Roldan, B. J. Kirby, D. Lee, Z. Liao, T. Charlton, A. Herklotz, T. Z. Ward, M. R. Fitzsimmons, and H. N. Lee, Sci. Adv. **5**, eaav5050 (2019).

[2] V. Nagarajan, A. Roytburd, A. Stanishevsky, S. Prasertchoung, T. Zhao, L. Chen, J. Melngailis, O. Auciello, and R. Ramesh, Nat. Mater. **2**, 43 (2003).

[3] E. K. H. Salje, Annu. Rev. Mater. Res. **42**, 265 (2012).

[4] Y. Tokura, Y. Tomioka, H. Kuwahara, A. Asamitsu, Y. Moritomo, and M. Kasai, J. Appl. Phys. **79**, 5288 (1996).

[5] Z. Liao, F. Li, P. Gao, L. Li, J. Guo, X. Pan, R. Jin, E. W. Plummer, and J. Zhang, Phys. Rev. B **92**, 125123 (2015).

[6] J.-C. Yang, Q. He, P. Yu, and Y.-H. Chu, Annu. Rev. Mater. Res. **45**, 249 (2015).

[7] U. Gebhardt, N. V. Kasper, A. Vigliante, P. Wochner, H. Dosch, F. S. Razavi, and H.-U. Habermeier, Phys. Rev. Lett. **98**, 096101 (2007).

[8] S. Jin, G. Gao, Z. Huang, Z. Yin, X. Zheng, and W. Wu, Appl. Phys. Lett. **92**, 261901 (2008).

[9] Y. H. Chu, Q. Zhan, L. W. Martin, M. P. Cruz, P. L. Yang, G. W. Pabst, F. Zavaliche, S. Y. Yang, J. X. Zhang, L. Q. Chen, D. G. Schlom, I.-N. Lin, T.-B. Wu, and R. Ramesh, Adv. Mater. **18**, 2307 (2006).

[10] T. Zhao, A. Scholl, F. Zavaliche, K. Lee, M. Barry, A. Doran, M. Cruz, Y. Chu, C. Ederer, N. Spaldin, R. R. Das, D. M. Kim, S. H. Baek, C. B. Eom, and R. Ramesh, Nat. Mater. **5**, 823 (2006).

[11] F. Sandiumenge, J. Santiso, L. Balcells, Z. Konstantinovic, J. Roqueta, A. Pomar, J. P. Espinós, and B. Martínez, Phys. Rev. Lett. **110**, 107206 (2013).

[12] H. W. Jang, D. Ortiz, S.-H. Baek, C. M. Folkman, R. R. Das, P. Shafer, Y. Chen, C. T. Nelson, X. Pan, R. Ramesh, and C.-B. Eom, Adv. Mater. **21**, 817 (2009).

[13] V. Shelke, D. Mazumdar, G. Srinivasan, A. Kumar, S. Jesse, S. Kalinin, A. Baddorf, and A. Gupta, Adv. Mater. **23**, 669 (2011).

[14] Y. Tokura and N. Nagaosa, Science **288**, 462 (2000).

[15] E. Dagotto, Science **309**, 257 (2005).

[16] P. Zubko, S. Gariglio, M. Gabay, P. Ghosez, and J.-M. Triscone, Annu. Rev. Condens. Matter Phys. **2**, 141 (2011).

[17] A. Bhattacharya and S. J. May, Annu. Rev. Mater. Res. **44**, 65 (2014).

[18] S. Stemmer and S. J. Allen, Annu. Rev. Mater. Res. **44**, 151 (2014).

[19] A. Ohtomo and H. Hwang, Nature (London) **427**, 423 (2004).

[20] M. Gibert, P. Zubko, R. Scherwitzl, J. Íñiguez, and J.-M. Triscone, Nat. Mater. **11**, 195 (2012).

[21] J. Zang, G. Zhou, Y. Bai, Z. Quan, and X. Xu, Sci. Rep. **7**, 10557 (2017).

[22] J. M. Hu, L. Q. Chen, and C. W. Nan, Adv. Mater. **28**, 15 (2016).

[23] X. Yu, L. Wu, B. Zhang, H. Zhou, Y. Dong, X. Wu, R. Kou, P. Yang, J. Chen, C.-J. Sun, Y. Zhu, and G. M. Chow, Phys. Rev. B **100**, 104405 (2019).

[24] M. Ziese, I. Vrejoiu, E. Pippel, P. Esquinazi, D. Hesse, C. Etz, J. Henk, A. Ernst, I. V. Maznichenko, W. Hergert, and I. Mertig, Phys. Rev. Lett. **104**, 167203 (2010).

[25] S. Das, A. Herklotz, E. Pippel, E. J. Guo, D. Rata, and K. Dörr, Phys. Rev. B **91**, 134405 (2015).

[26] D. G. Schlom, L.-Q. Chen, C.-B. Eom, K. M. Rabe, S. K. Streiffer, and J.-M. Triscone, Annu. Rev. Mater. Res. **37**, 589 (2007).

[27] F. Johann, A. Morelli, D. Biggemann, M. Arredondo, and I. Vrejoiu, Phys. Rev. B **84**, 094105 (2011).

[28] J. M. Rondinelli, S. J. May, and J. W. Freeland, MRS Bull. **37**, 261 (2012).

[29] J. M. Rondinelli and N. A. Spaldin, Adv. Mater. **23**, 3363 (2011).

[30] C. L. Jia, S. B. Mi, M. Faley, U. Poppe, J. Schubert, and K. Urban, Phys. Rev. B **79**, 081405(R) (2009).

[31] E. Moon, P. Balachandran, B. J. Kirby, D. Keavney, R. Sichel-Tissot, C. Schleputz, E. Karapetrova, X. Cheng, J. M. Rondinelli, and S. May, Nano Lett. **14**, 2509 (2014).

[32] J.-H. Park, E. Vescovo, H.-J. Kim, C. Kwon, R. Ramesh, and T. Venkatesan, Nature (London) **392**, 794 (1998).

[33] A. P. Ramirez, J. Phys.: Condens. Matter **9**, 8171 (1997).

[34] S. J. Hibble, S. P. Cooper, A. C. Hannon, I. D. Fawcett, and M. Greenblatt, J. Phys.: Condens. Matter **11**, 9221 (1999).

[35] See Supplemental Material at http://link.aps.org/supplemental/10.1103/PhysRevB.104.125423 for the illustrations of biaxial strain and shear strain in ferroelastic films, layer-by-layer growth of the LSMO thin films, confirmation of the unidirectional long-range modulation in LSMO/ film, domain structure in LSMO films grown on substrates, origin of the reflection patterns in RSMs of LSMO films grown on substrates, relationship between unit-cell tilting direction and rotation signs network, RSMs of LSMO films grown on NGO substrates with various thicknesses, magnetotransport properties of LSMO films, estimation of the MAE of LSMO films grown on NGO substrates, domain structure and magnetic anisotropy in STO-buffered LSMO films, and XAS, XLD, and ALD results at Mn L edge for LSMO films.

[36] N. Farag, M. Bobeth, W. Pompe, A. Romanov, and J. Speck, J. Appl. Phys. **97**, 113516 (2005).

[37] J.-L. Maurice, F. Pailloux, A. Barthélémy, O. Durand, D. Imhoff, R. Lyonnet, A. Rocher, and J.-P. Contour, Philos. Mag. **83**, 3201 (2003).

[38] O. Lebedev, G. V. Tendeloo, S. Amelinckx, H. Ju, and K. M. Krishnan, Philos. Mag. A **80**, 673 (2000).

[39] S. H. Seo, H. C. Kang, H. W. Jang, and D. Y. Noh, Phys. Rev. B **71**, 012412 (2005).

[40] B. Paudel, B. Zhang, Y. Sharma, K. T. Kang, H. Nakotte, H. Wang, and A. Chen, Appl. Phys. Lett. **117**, 081903 (2020).

[41] A. Vailionis, H. Boschker, W. Siemons, E. P. Houwman, D. H. A. Blank, G. Rijnders, and G. Koster, Phys. Rev. B **83**, 064101 (2011).

[42] M. Marezio, J. Remeika, and P. Dernier, Inorg. Chem. **7**, 1337 (1968).

[43] P. G. Radaelli, G. Iannone, M. Marezio, H. Y. Hwang, S. W. Cheong, J. D. Jorgensen, and D. N. Argyriou, Phys. Rev. B **56**, 8265 (1997).

[44] J. Santiso, L. Balcells, Z. Konstantinovic, J. Roqueta, P. Ferrer, A. Pomar, B. Martínez, and F. Sandiumenge, CrystEngComm **15**, 3908 (2013).

[45] Z. Chen, A. Damodaran, R. Xu, S. Lee, and L. Martin, Appl. Phys. Lett. **104**, 182908 (2014).

[46] A. Glazer, Acta Crystallogr. A **31**, 756 (1975).

[47] Z. Liao, R. J. Green, N. Gauquelin, S. Macke, L. Li, J. Gonnissen, R. Sutarto, E. P. Houwman, Z. Zhong, S. Van Aert, J. Verbeeck, G. A. Sawatzky, M. Huijben, G. Koster, and G. Rijnders, Adv. Funct. Mater. **26**, 6627 (2016).

[48] Z. Liao, M. Huijben, Z. Zhong, N. Gauquelin, S. Macke, R. Green, S. Van Aert, J. Verbeeck, G. Van Tendeloo, K. Held, G. A. Sawatzky, G. Koster, and G. Rijnders, Nat. Mater. **15**, 425 (2016).

[49] D. Kan, R. Aso, R. Sato, M. Haruta, H. Kurata, and Y. Shimakawa, Nat. Mater. **15**, 432 (2016).

[50] D. Yi, C. L. Flint, P. P. Balakrishnan, K. Mahalingam, B. Urwin, A. Vailionis, A. T. NDiaye, P. Shafer, E. Arenholz, Y. Choi, K. H. Stone, J.-H. Chu, B. M. Howe, J. Liu, I. R. Fisher, and Y. Suzuki, Phys. Rev. Lett. **119**, 077201 (2017).

[51] P. Chen, Z. Huang, M. Li, X. Yu, X. Wu, C. Li, N. Bao, S. Zeng, P. Yang, L. Qu, J. Chen, J. Ding, S. J. Pennycook, W. Wu, T. V.

Venkatesan, A. Ariando, and G. M. Chow, Adv. Funct. Mater. **30**, 1909536 (2020).

[52] Y. Suzuki, H. Hwang, S.-W. Cheong, and R. Van Dover, Appl. Phys. Lett. **71**, 140 (1997).

[53] D. Yi, J. Liu, S.-L. Hsu, L. Zhang, Y. Choi, J.-W. Kim, Z. Chen, J. D. Clarkson, C. R. Serrao, E. Arenholz, P. J. Ryang, H. Xu, R. J. Birgeneaua, and R. Ramesh, Proc. Natl. Acad. Sci. **113**, 6397 (2016).

[54] Z. Guo, D. Lan, L. Qu, K. Zhang, F. Jin, B. Chen, S. Jin, G. Gao, F. Chen, L. Wang, and W. Wu, Appl. Phys. Lett. **113**, 231601 (2018).

[55] A. Rajapitamahuni, L. L. Tao, Y. Hao, J. Song, X. Xu, E. Y. Tsymbal, and X. Hong, Phys. Rev. Mater. **3**, 021401(R) (2019).

[56] C. Schlueter, N. Yang, C. Mazzoli, C. Cantoni, A. Tebano, D. Di Castro, G. Balestrino, P. Orgiani, A. Galdi, J. Herrero-Martín, P. Gargiani, M. Valvidares, and C. Aruta, Adv. Quantum Technol. **3**, 2000016 (2020).

[57] M. Huijben, L. W. Martin, Y.-H. Chu, M. B. Holcomb, P. Yu, G. Rijnders, D. H. A. Blank, and R. Ramesh, Phys. Rev. B **78**, 094413 (2008).

[58] L. F. Kourkoutis, J. Song, H. Hwang, and D. Muller, Proc. Natl. Acad. Sci. **107**, 11682 (2010).

[59] H. Boschker, M. Mathews, E. P. Houwman, H. Nishikawa, A. Vailionis, G. Koster, G. Rijnders, and D. H. A. Blank, Phys. Rev. B **79**, 214425 (2009).

[60] O. Thomas, Q. Shen, P. Schieffer, N. Tournerie, and B. Lépine, Phys. Rev. Lett. **90**, 017205 (2003).

[61] I. Infante, J. Ossó, F. Sánchez, and J. Fontcuberta, Appl. Phys. Lett. **92**, 012508 (2008).

[62] D. Pesquera, G. Herranz, A. Barla, E. Pellegrin, F. Bondino, E. Magnano, F. Sánchez, and J. Fontcuberta, Nat. Commun. **3**, 1189 (2012).

[63] A. Tebano, C. Aruta, S. Sanna, P. G. Medaglia, G. Balestrino, A. A. Sidorenko, R. De Renzi, G. Ghiringhelli, L. Braicovich, V. Bisogni, and N. B. Brookes, Phys. Rev. Lett. **100**, 137401 (2008).

[64] D. Preziosi, M. Alexe, D. Hesse, and M. Salluzzo, Phys. Rev. Lett. **115**, 157401 (2015).

[65] D. Pesquera, A. Barla, M. Wojcik, E. Jedryka, F. Bondino, E. Magnano, S. Nappini, D. Gutiérrez, G. Radaelli, G. Herranz, F. Sánchez, and J. Fontcuberta, Phys. Rev. Appl. **6**, 034004 (2016).

[66] Z. Liao, N. Gauquelin, R. J. Green, S. Macke, J. Gonnissen, S. Thomas, Z. Zhong, L. Li, L. Si, S. Van Aert, P. Hansmann, K. Held, J. Xia, J. Verbeeck, G. V. Tendeloo, G. A. Sawatzky, G. Koster, M. Huijben, and G. Rijnders, Adv. Funct. Mater. **27**, 1606717 (2017).

[67] J. M. De Teresa, M. R. Ibarra, J. Blasco, J. Garcia, C. Marquina, P. A. Algarabel, Z. Arnold, K. Kamenev, C. Ritter, and R. von Helmolt, Phys. Rev. B **54**, 1187 (1996).

[68] S. J. May, J.-W. Kim, J. M. Rondinelli, E. Karapetrova, N. A. Spaldin, A. Bhattacharya, and P. J. Ryan, Phys. Rev. B **82**, 014110 (2010).

[69] A. J. Hatt and N. A. Spaldin, Phys. Rev. B **82**, 195402 (2010).

[70] Z. Liao, Z. Li, and J. Zhu, J. Am. Ceram. Soc. **99**, 3734 (2016).